Ozone seasonal evolution and photochemical production regime in polluted troposphere in eastern China derived from high resolution FTS observations

Youwen Sun [1, 2)#], Cheng Liu [2, 3, 1)#*], Mathias Palm [4)], Corinne Vigouroux [5)], Justus Notholt [4)], Qihou Hu [1)], Nicholas Jones [6)], Wei Wang [1)], Wenjing Su [3)] , Wenqiang Zhang [3)], Changong Shan [1)], Yuan Tian [1)], Xingwei, Xu [1)], Martine De Mazière [5)], Minqiang Zhou [5)] and Jianguo Liu [1)]

(1 *Key Laboratory of Environmental Optics and Technology, Anhui Institute of Optics and Fine Mechanics, Chinese Academy of Sciences, Hefei 230031, China*)

(2 *Center for Excellence in Urban Atmospheric Environment, Institute of Urban Environment, Chinese Academy of Sciences, Xiamen 361021, China*)

(3 *University of Science and Technology of China, Hefei, 230026, China*)

(4 *University of Bremen, Institute of Environmental Physics, P. O. Box 330440, 28334 Bremen, Germany*)

(5 *Royal Belgian Institute for Space Aeronomy (BIRA-IASB), Brussels, Belgium*)

(6 *School of Chemistry, University of Wollongong, Northfields Ave, Wollongong, NSW, 2522, Australia*)

# These two authors contributed equally to this work

Abstract:

The seasonal evolution of O_3 and its photochemical production regime in a polluted region of eastern China between 2014 and 2017 has been investigated using different observations and modelling. We used tropospheric ozone (O_3), carbon monoxide (CO) and formaldehyde (HCHO, a marker of VOCs (volatile organic compounds)) partial columns derived from high resolution Fourier transform spectrometry (FTS), tropospheric nitrogen dioxide (NO_2, a marker of NOx (nitrogen oxides)) partial column deduced from Ozone Monitoring Instrument (OMI), surface meteorological data, and a back trajectory cluster analysis technique. A broad O_3 maximum during both spring and summer (MAM/JJA) is observed; the day-to-day variations in MAM/JJA are generally larger than those in autumn and winter

Correspondence to: Cheng Liu (chliu81@ustc.edu.cn) or Youwen Sun (ywsun@aiofm.ac.cn)

(SON/DJF). Tropospheric O_3 columns in June are, on average, 0.50×10^{18} molecules*cm^{-2} (47.6%) higher than those in December which has a mean value of 1.05×10^{18} molecules*cm^{-2}. Compared with SON/DJF season, the observed tropospheric O_3 levels in MAM/JJA are mainly influenced by transport of air masses from densely populated and industrialized areas while the broad and high O_3 level and variability in MAM/JJA is determined by the photochemical O_3 production. The tropospheric column HCHO/NO_2 ratio is used as a proxy to investigate the photochemical O_3 production rate (PO_3). The results show that the PO_3 is mainly nitrogen oxides (NO_x) limited in MAM/JJA, while it is mainly VOC or mix VOC-NO_x limited in SON/DJF. Statistics show that NO_x limited, mix VOC-NO_x limited, and VOC limited PO_3 accounts for 60.1%, 28.7%, and 11%, respectively. Considering most of PO_3 are NO_x limited or mix VOC-NO_x limited, reductions in NO_x would reduce most of the O_3 pollution in eastern China.

1 Introduction

Human health, terrestrial ecosystems, and materials degradation are impacted by poor air quality resulting from high photochemical ozone (O_3) levels (Wennberg and Dabdub, 2008; Edwards et al., 2013; Schroeder et al., 2017). In polluted areas, tropospheric O_3 generates from a series of complex reactions in the presence of sunlight involving carbon monoxide (CO), nitrogen oxides ($NO_x \equiv$ NO (nitric oxide) + NO_2 (nitrogen dioxide)), and volatile organic compounds (VOCs) (Oltmans et al., 2006; Schroeder et al., 2017). Briefly, VOCs first react with the hydroxyl radical (OH) to form a peroxy radical ($HO_2 + RO_2$) which increases the rate of catalytic cycling of NO to NO_2. O_3 is then produced by subsequent reactions between HO_2 or RO_2 and NO that lead to radical propagation (via subsequent reformation of OH). Radical termination proceeds via reaction of OH with NOx to form nitric acid (HNO_3) (reaction (1), referred to as LNOx) or by radical-radical reactions resulting in stable peroxide formation (reactions (2) − (4), referred to as LROx, where ROx $\equiv RO_2 + HO_2$) (Schroeder et al., 2017):

$$OH + NO_2 \rightarrow HNO_3 \tag{1}$$

$$2HO_2 \rightarrow H_2O_2 + O_2 \tag{2}$$

$$60 \qquad HO_2 + RO_2 \rightarrow ROOH + O_2 \qquad (3)$$

$$61 \qquad 2RO_2 \rightarrow ROOR + O_2 \qquad (4)$$
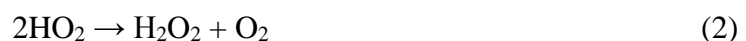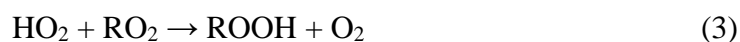
62 Typically, the relationship between these two competing radical termination processes

63 (referred to as the ratio LRO_x/LNO_x) can be used to evaluate the photochemical

64 regime. In high-radical, low-NO_x environments, reactions (2) – (4) remove radicals at

65 a faster rate than reaction (1) (i.e., LROx $\gg$ LNOx), and the photochemical regime is

66 regarded as "NOx limited". In low-radical, high-NOx environments the opposite is

67 true (i.e., LROx $\ll$ LNOx) and the regime is regarded as "VOC limited". When the

68 rates of the two loss processes are comparable (LNOx $\approx$ LROx), the regime is said to

69 be at the photochemical transition/ambiguous point, i.e., mix VOC-NOx limited

70 (Kleinman et al., 2005; Sillman et al., 1995a; Schroeder et al., 2017).

71 Understanding the photochemical regime at local scales is a crucial piece of

72 information for enacting effective policies to mitigate O_3 pollution (Jin et al., 2017;

73 Schroeder et al., 2017). In order to determine the regime, the total reactivity with OH

74 of the myriad of VOCs in the polluted area has to be estimated (Sillman, 1995a; Xing

75 et al., 2017). In the absence of such information, the formaldehyde (HCHO)

76 concentration can be used as a proxy for VOC reactivity because it is a short-lived

77 oxidation product of many VOCs and is positively correlated with peroxy radicals

78 (Schroeder et al., 2017). Sillman (1995a) and Tonnesen and Dennis (2000) found that

79 in situ measurements of the ratio of HCHO (a marker of VOCs) to NO_2 (a marker of

80 NOx) could be used to diagnose local photochemical regimes. Over polluted areas,

81 both HCHO and tropospheric NO_2 have vertical distributions that are heavily

82 weighted toward the lower troposphere, indicating that tropospheric column

83 measurements of these gases are fairly representative of near surface conditions.

84 Many studies have taken advantage of these favorable vertical distributions to

85 investigate surface emissions of NOx and VOCs from space (Boersma et al., 2009;

86 Martin et al., 2004a; Millet et al., 2008; Streets et al., 2013). Martin et al. (2004a) and

87 Duncan et al. (2010) used satellite measurements of column HCHO/NO_2 ratio to

88 explore near-surface O_3 sensitivities from space and disclosed that this diagnosis of

89 O_3 production rate (PO$_3$) is consistent with previous finding of surface photochemistry.

90 Witte et al. (2011) used the similar technique to estimate changes in PO_3 to the strict

91 emission control measures (ECMs) during Beijing Summer Olympic Games period in

92 2008. Recent papers have applied the findings of Duncan et al. (2010) to observe O_3

93 sensitivity in other parts of the world (Choi et al., 2012; Witte et al., 2011; Jin and

94 Holloway, 2015; Mahajan et al., 2015; Jin et al., 2017).

95   With in situ measurements, Tonnesen and Dennis (2000) observed a

96 radical-limited environment with $HCHO/NO_2$ ratios < 0.8, a NOx-limited

97 environment with $HCHO/NO_2$ ratios >1.8, and a transition environment with

98 $HCHO/NO_2$ ratios between 0.8 and 1.8. With 3-d chemical model simulations,

99 Sillman (1995a) and Martin et al. (2004b) estimated that the transition between the

100 VOC- and NO_x-limited regimes occurs when the $HCHO/NO_2$ ratio is ~ 1.0. With a

101 combination of regional chemical model simulations and the Ozone Monitoring

102 Instrument (OMI) measurements, Duncan et al. (2010) concluded that O_3 production

103 decreases with reductions in VOCs at column $HCHO/NO_2$ ratio < 1.0 and NO_x at

104 column $HCHO/NO_2$ ratio > 2.0; both NO_x and VOCs reductions decrease O_3

105 production when column $HCHO/NO_2$ ratio lies in between 1.0 and 2.0. With a 0-D

106 photochemical box model and airborne measurements, Schroeder et al. (2017)

107 presented a thorough analysis of the utility of column $HCHO/NO_2$ ratios to indicate

108 surface O_3 sensitivity and found that the transition/ambiguous range estimated via

109 column data is much larger than that indicated by in situ data alone. Furthermore,

110 Schroeder et al. (2017) concluded that many additional sources of uncertainty

111 (regional variability, seasonal variability, variable free tropospheric contributions,

112 retrieval uncertainty, air pollution levels and meteorological conditions) may cause

113 transition threshold vary both geographically and temporally, and thus the results from

114 one region are not likely to be applicable globally.

115   With the rapid increase in fossil fuel consumption in China over the past three

116 decades, the emission of chemical precursors of O_3 (NO_x and VOCs) has increased

117 dramatically, surpassing that of North America and Europe and raising concerns about

118 worsening O_3 pollution in China (Tang et al., 2011; Wang et al., 2017; Xing et al.,

119 2017). Tropospheric O_3 was already included in the new air quality standard as a

routine monitoring component (http://www.mep.gov.cn, last access on 23 May 2018), where the limit for the maximum daily 8 h average (MDA8) O_3 in urban and industrial areas is 160μg/m^3 (~ 75 ppbv at 273 K, 101.3 kPa). According to air quality data released by the Chinese Ministry of Environmental Protection, tropospheric O_3 has displaced PM2.5 as the primary pollutant in many cities during summer (http://www.mep.gov.cn/, last access on 23 May 2018). A precise knowledge of O_3 evolution and photochemical production regime in polluted troposphere in China has important policy implications for O_3 pollution controls (Tang et al., 2011; Xing et al., 2017; Wang et al., 2017).

In this study, we investigate O_3 seasonal evolution and photochemical production regime in the polluted troposphere in eastern China with tropospheric O_3, CO and HCHO derived from ground-based high resolution Fourier transform spectrometry (FTS) in Hefei, China, tropospheric NO_2 deduced from the OMI satellite (https://aura.gsfc.nasa.gov/ omi.html, last access on 23 May 2018), surface meteorological data, and a back trajectory cluster analysis technique. Considering the fact that most NDACC (Network for Detection of Atmospheric Composition Change) FTS sites are located in Europe and Northern America, whereas the number of sites in Asia, Africa, and South America is very sparse, and there is still no official NDACC FTS station that covers China (http://www.ndacc.org/, last access on 23 May 2018), this study can not only improve our understanding of regional photochemical O_3 production regime, but also contributes to the evaluation of O_3 pollution controls.

This study is organized as below: in section 2 the location and the instrument is described, section 3 describes the retrieval of the gases. In section 4, the tropospheric evolution of O_3 in Hefei is investigated. In section 5, the production regimes are evaluated. The work concludes with a summary in section 6.

2 Site description and instrumentation

The FTS observation site (117°10′E, 31°54′N, 30 m a.s.l. (above sea level)) is located in the western suburbs of Hefei city (the capital of Anhui Province, 8 million population) in central-eastern China (Figure S1). Detailed description of this site and

149   its typical observation scenario can be found in Tian et al. (2018). Similar to other

150   Chinese megacities, serious air pollution is common in Hefei throughout the whole

151   year (http://mep.gov.cn/, last access on 23 May 2018).

152   Our observation system consists of a high resolution FTS spectrometer

153   (IFS125HR, Bruker GmbH, Germany), a solar tracker (Tracker-A Solar 547, Bruker

154   GmbH, Germany), and a weather station (ZENO-3200, Coastal Environmental

155   Systems, Inc., USA). The near infrared (NIR) and middle infrared (MIR) solar spectra

156   were alternately acquired in routine observations (Wang et al., 2017). The MIR

157   spectra used in this study are recorded over a wide spectral range (about $600 - 4500$

158   cm^{-1}) with a spectral resolution of $0.005 cm^{-1}$. The instrument is equipped with a KBr

159   beam splitter & MCT detector for O_3 measurements and a KBr beam splitter & InSb

160   detector for other gases. The weather station includes sensors for air pressure ($\pm$

161   0.1hpa), air temperature ($\pm 0.3 \,^{\circ}C$), relative humidity ($\pm 3\%$), solar radiation ($\pm 5\%$),

162   wind speed (± 0.2 m/s), wind direction ($\pm 5 \,^{\circ}$), and the presence of rain.

3 FTS retrievals of O_3, CO and HCHO

3.1 Retrieval strategy

165   The SFIT4 (version 0.9.4.4) algorithm is used in the profile retrieval (Supplement

166   section A; https://www2.acom.ucar.edu/irwg/links, last access on 23 May 2018). The

167   retrieval settings for O_3, CO, and HCHO are listed in Table 1. All spectroscopic line

168   parameters are adopted from HITRAN 2008 (Rothman et al., 2009). A priori profiles

169   of all gases except H_2O are from a dedicated WACCM (Whole Atmosphere

170   Community Climate Model) run. A priori profiles of pressure, temperature and H_2O

171   are interpolated from the National Centers for Environmental Protection and National

172   Center for Atmospheric Research (NCEP/NCAR) reanalysis (Kalnay et al., 1996). For

173   O_3 and CO, we follow the NDACC standard convention with respect to micro

174   windows (MW) selection and the interfering gases consideration (https://www2.acom.

175   ucar.edu/irwg/links, last access on 23 May 2018). HCHO is not yet an official

176   NDACC species but has been retrieved at a few stations with different retrieval

177   settings (Albrecht et al., 2002; Vigouroux et al., 2009; Jones et al., 2009; Viatte et al.,

178   2014; Franco et al., 2015). The four MWs used in the current study are chosen from a

179   harmonization project taking place in view of future satellite validation (Vigouroux et

180 al., 2018). They are centered at around 2770 cm^{-1} and the interfering gases are CH_4,

181 O_3, N_2O, and HDO.

182 We assume measurement noise covariance matrices $\mathbf{S}_\varepsilon$ to be diagonal, and set its

183 diagonal elements to the inverse square of the signal to noise ratio (SNR) of the fitted

184 spectra and its non-diagonal elements to zero. For all gases, the diagonal elements of

185 *a priori* profile covariance matrices $\mathbf{S}_a$ are set to standard deviation of a dedicated

186 WACCM run from 1980 to 2020, and its non-diagonal elements are set to zero.

187 We regularly used a low-pressure HBr cell to monitor the instrument line shape

188 (ILS) of the instrument and included the measured ILS in the retrieval (Hase et al.,

189 2012; Sun et al., 2018).

190 **3.2 Profile information in the FTS retrievals**

191 The sensitive range for CO and HCHO is mainly tropospheric, and for O_3 is both

192 tropospheric and stratospheric (Figure S2). The typical degrees of freedom (DOFS)

193 over the total atmosphere obtained in Hefei for each gas are included in Table 2: they

194 are about 4.8, 3.5, and 1.2 for O_3, CO, and HCHO, respectively. In order to separate

195 independent partial column amounts in the retrieved profiles, we have chosen the

196 altitude limit for each independent layer such that the DOFS in each associated partial

197 column is not less than 1.0. The retrieved profiles of O_3, CO, and HCHO can be

198 divided into four, three, and one independent layers, respectively (Figure S3). The

199 troposphere is well resolved by O_3, CO, and HCHO, where CO exhibits the best

200 vertical resolution with more than two independent layers in the troposphere.

201 In this study, we have chosen the same upper limit for the tropospheric columns

202 for all gases, which is about 3 km lower than the mean value of the tropopause (~15.1

203 km). In this way we ensured the accuracies for the tropospheric O_3, CO, and HCHO

204 retrievals, and minimized the influence of transport from stratosphere, i.e., the so

205 called STE process (stratosphere-troposphere exchange).

206 **3.3 Error analysis**

207 The results of the error analysis presented here based on the average of all

208 measurements that fulfill the screening scheme, which is used to minimize the impacts

209 of significant weather events or instrument problems (Supplement section B). In the

210 troposphere, the dominant systematic error for O_3 and CO is the smoothing error, and

211 for HCHO is the line intensity error (Figure S4). The dominant random error for O_3

and HCHO is the measurement error, and for CO is the zero baseline level error (Figure S5). Taken all error items into account, the summarized errors in O_3, CO, and HCHO for 0 −12 km tropospheric partial column and for the total column are listed in Table 3. The total errors in the tropospheric partial columns for O_3, CO, and HCHO, have been evaluated to be 8.7%, 6.8%, and 10.2%, respectively.

4 Tropospheric O_3 seasonal evolution

4.1 Tropospheric O_3 seasonal variability

Figure 1(a) shows the tropospheric O_3 column time series recorded by the FTS from 2014 to 2017, where we followed Gardiner's method and used a second-order Fourier series plus a linear component to determine the annual variability (Gardiner et al., 2008). While it failed to determine the secular trend of tropospheric O_3 column probably because the time series is much shorter than those in Gardiner et al. (2008), the observed seasonal cycle of tropospheric O_3 variations is well captured by the bootstrap resampling method (Gardiner et al., 2008). As commonly observed, high levels of tropospheric O_3 occur in spring and summer (hereafter MAM/JJA). Low levels of tropospheric O_3 occur in autumn and winter (hereafter SON/DJF). Day-to-day variations in MAM/JJA are generally larger than those in SON/DJF (Figure 1(b)). At the same time, it shows that the tropospheric O_3 column roughly increases over time at the first half of the year and reaches the maximum in June, and then decreases during the second half of the year. Tropospheric O_3 columns in June were, on average, 0.5×10^{18} molecules*cm^{-2} (47.6%) higher than those in December which have a mean value of 1.05×10^{18} molecules*cm^{-2}.

Vigouroux et al. (2015) studied the O_3 trends and variabilities at eight NDACC FTS stations that have a long-term time series of O_3 measurements, namely, Ny-Ålesund (79 °N), Thule (77 °N), Kiruna (68 °N), Harestua (60 °N), Jungfraujoch (47 °N), Izaña (28 °N), Wollongong (34 °S) and Lauder (45 °S). All these stations were located in non-polluted or relatively clean areas. The results showed a maximum tropospheric O_3 column in spring at all stations except at Jungfraujoch where it extended into summer. This is because the STE process is most effective during late

241   winter and spring (Vigouroux et al. 2015). In contrast, we observed a broader

242   maximum in Hefei which extends over MAM/JJA season, and the values are higher

243   than those studied in Vigouroux et al. (2015). This is because the observed

244   tropospheric O_3 levels in MAM/JJA are more influenced by air masses originated

245   from densely populated and industrialized areas (see section 4.2), and the MAM/JJA

246   meteorological conditions are more favorable to photochemical O_3 production (see 6).

247   The selection of tropospheric limits 3 km below the tropopause minimized but cannot

248   avoid the influence of transport from stratosphere, the STE process may also

249   contribute to high level of tropospheric O_3 column in spring. Particularly, there is no

250   stronger signature of summer O_3 enhancements in Hefei is most probably because the

251   STE process is weaker in summer than in spring (Vigouroux et al. 2015).

4.2 Regional contribution to tropospheric O_3 levels

253   In order to determine where the air masses came from and thus contributed to the

254   observed tropospheric O_3 levels, we have used the HYSPLIT (Hybrid Single-Particle

255   Lagrangian Integrated Trajectory) model to calculate the three-dimensional kinematic

256   back trajectories that coincide with the FTS measurements from 2014 - 2017 (Draxler

257   et al., 2009). In the calculation, the GDAS (University of Alaska Fairbanks GDAS

258   Archive) meteorological fields were used with a spatial resolution of 0.25 °× 0.25 °, a

259   time resolution of 6 h and 22 vertical levels from the surface to 250 mbar. All daily

260   back trajectories at 12:00 UTC, with a 24 h pathway arriving at Hefei site at 1500 m

261   a.s.l., have been grouped into clusters, and divided into MAM/JJA and SON/DJF

262   seasons (Stunder, 1996). The results showed that air pollution in Jiangsu and Anhui

263   Province in eastern China, Hebei and Shandong Province in northern China, Shaanxi,

264   Henan and Shanxi Province in northwestern China, Hunan and Hubei Province in

265   central China contributed to the observed tropospheric O_3 levels.

266   In MAM/JJA season (Figure 2(a)), 28.8% of air masses are east origin and arrived

267   at Hefei through the southeast of Jiangsu Province and east of Anhui Province; 41.0%

268   are southwest origin and arrived at Hefei through the northeast of Hunan and Hubei

269   Province, and southwest of Anhui Province; 10.1% are northwest origin and arrived at

270 Hefei through the southeast of Shanxi and Henan Province, and northwest of Anhui

271 Province; 10.1% are north origin and arrived at Hefei through the south of Shandong

272 Province and north of Anhui Province; 10.1% are local origin generated in south of

273 Anhui Province. As a result, air pollution from megacities such as Shanghai, Nanjing,

274 Hangzhou and Hefei in eastern China, Changsha and Wuhan in central-southern

275 China, Zhenzhou and Taiyuan in northwest China, and Jinan in north China could

276 dominate the contribution to the observed tropospheric O_3 levels.

277  In SON/DJF season, air masses are generally longer and originated in the

278 northwest of the MAM/JJA ones (Figure 2(b)). The direction of east origin air masses

279 shifts from the southeast to northeast of Jiangsu Province, and that of local origin air

280 masses shifts from the south to the northwest of Anhui province. Trajectories of east

281 origin, west origin, and north origin air masses in SON/DJF are 6.5%, 13.1%, and

282 0.7% smaller than the MAM/JJA ones, respectively. As a result, the air pollution

283 outside Anhui province have 20.2% smaller contribution to the observed tropospheric

284 O_3 levels in SON/DJF than in MAM/JJA. In contrast, trajectories of local origin air

285 masses in SON/DJF are 20.2% larger than the MAM/JJA ones, indicating a more

286 significant contribution of the air pollution inside Anhui province in SON/DJF.

287  The majority of the Chinese population lives in the eastern part of China,

288 especially in the three most developed regions, the Jing-Jin-Ji (Beijing-Tianjin-Hebei),

289 the Yangtze River Delta (YRD; including Shanghai-Jiangsu-Zhejiang-Anhui), and the

290 Pearl River Delta (PRD; including Guangzhou, Shenzhen, and Hong Kong). These

291 regions consistently have the highest emissions of anthropogenic precursors (Figure

292 S6), which have led to severe region-wide air pollution. Particularly, the Hefei site

293 located in the central-western corner of the YRD, where the population in the

294 southeastern area is typically denser than the northwestern area. Specifically, the

295 southeast of Jiangsu province and the south of Anhui province are two of the most

296 developed areas in YRD, and human activities therein are very intense. Therefore,

297 when the air masses originated from these two areas, O_3 level is usually very high.

298 Overall, compared with SON/DJF season, the more southeastern air masses

299 transportation in MAM/JJA indicated that the observed tropospheric O_3 levels could

300   be more influenced by the densely populated and industrialized areas, which can be

301   broadly accounting for higher O_3 level and variability in MAM/JJA.

5 Tropospheric O_3 production regime

5.1 Meteorological dependency

304   Photochemistry in polluted atmospheres, particularly the formation of O_3,

305   depends not only on pollutant emissions, but also on meteorological conditions (Lei et

306   al., 2008; Wang et al., 2016; Coates et al., 2016). In order to investigate

307   meteorological dependency of O_3 production regime in the observed area, we

308   analyzed the correlation of the tropospheric O_3 with the coincident minutely-averaged

309   surface meteorological data. Figure 3 shows time series of temperature, pressure,

310   humidity, wind direction, wind speed, and solar radiation recorded by the surface

311   weather station. The seasonal dependencies of all these coincident meteorological

312   elements show no clear dependencies except for the temperature and pressure which

313   show clear reverse seasonal cycles. Generally, the temperatures are higher and the

314   pressures are lower in MAM/JJA than those in SON/DJF. The correlation plots

315   between FTS tropospheric O_3 column and each meteorological element are shown in

316   Figure 4. The tropospheric O_3 column shows positive correlations with solar radiation

317   and temperature, and negative correlations with pressure, humidity, wind direction

318   and wind speed.

319   High temperature and strong sunlight primarily affects O_3 production in Hefei in

320   two ways: speeding up the rates of many chemical reactions and increasing emissions

321   of VOCs from biogenic sources (BVOCs) (Sillman and Samson, 1995b). While

322   emissions of anthropogenic VOCs (AVOCs) are generally not dependent on

323   temperature, evaporative emissions of some AVOCs do increase with temperature

324   (Rubin et al., 2006; Coates et al., 2016). Elevated O_3 concentration generally occurs

325   on days with dry condition, low pressure and low winds in Hefei probably because

326   these conditions favor the accumulation of O_3 and its precursors. Wind direction is

327   also important because it affects pollution transport, giving rise to high O_3 in

328   downwind locations (Wang et al., 2016). The city downtown locates in eastern of the

329 observation site and the majority of the Chinese population lives in the eastern part of

330 China, easterly winds (direction less than 180˚) could generally transport more

331 pollutants to the observe area than westerly winds (direction larger than 180˚),

332 resulting in a higher O_3 level. Overall, MAM/JJA meteorological conditions are more

333 favorable to O_3 production (higher sun intensity, higher temperature, lower pressure,

334 and more easterly winds) than SON/DJF, which consolidates the fact that tropospheric

335 O_3 in MAM/JJA are larger than those in SON/DJF.

336 ## 5.2 PO_3 relative to CO, HCHO, and NO_2 changes

337 In order to determine the relationship between tropospheric O_3 production and its

338 precursors, the chemical sensitivity of PO_3 relative to tropospheric CO, HCHO, and

339 NO_2 changes was investigated. Figure 5 shows time series of tropospheric CO, HCHO,

340 and NO_2 columns stay at present tropospheric O_3 counterparts, where tropospheric

341 NO_2 was deduced from OMI product selected within the $\pm 0.7°$ latitude/longitude

342 rectangular area around Hefei site. The retrieval uncertainty for tropospheric column

343 of is less than 30% (https://disc.gsfc.nasa.gov/datasets/OMNO2_V003/). Similar as

344 tropospheric O_3, tropospheric HCHO exhibits a clear seasonal cycle and has a

345 minimum in winter and a maximum in summer. Pronounced tropospheric CO and

346 NO_2 variations were observed but the seasonal cycles are not evident probably

347 because of air pollution which is not constant over season or season dependent.

348 Figure 6 shows the correlation plot between the FTS tropospheric O_3 column and

349 the coincident tropospheric CO, HCHO, and NO_2 columns. The tropospheric O_3

350 column shows positive correlations with tropospheric CO, HCHO, and NO_2 columns.

351 Generally, the higher the tropospheric CO concentration, the higher the tropospheric

352 O_3, and both VOCs and NO_x reductions decrease O_3 production. As an indicator of

353 regional air pollution, the good correlation between O_3 and CO (Figure 6(a)) indicates

354 that the enhancement of tropospheric O_3 is highly associated with the photochemical

355 reactions which occurred in polluted conditions rather than due to the STE process.

356 Since the sensitivity of PO_3 to VOCs and NO_x is different under different limitation

357 regimes, the relative weaker overall correlations to HCHO (Figure 6 (b)) and NO_2

358 (Figure 6 (c)) indicates that the O_3 pollution in Hefei can neither be fully attributed to

359 NO_x pollution nor VOCs pollution.

360 **5.3 O_3-NOx-VOCs sensitivities**

361 **5.3.1 Transition/ambiguous range estimation**

362 Referring to previous studies, the chemical sensitivity of PO_3 in Hefei was

363 investigated using the column $HCHO/NO_2$ ratio (Martin et al., 2004; Duncan et al.,

364 2010; Witte et al., 2011; Choi et al., 2012; Jin and Holloway, 2015; Mahajan et al.,

365 2015; Schroeder et al., 2017; Jin et al., 2017). The methods have been adapted to the

366 particular conditions in Hefei. In particular the findings of Schroeder et.al (2017) have

367 been taken into account.

368 First, previous studies either based on space or airborne column $HCHO/NO_2$

369 ratios (Martin et al., 2004; Duncan et al., 2010; Witte et al., 2011; Schroeder et al.,

370 2017), both ground-based remote sensing (O_3, CO, and HCHO) and results measured

371 from space (NO_2) were used here. Both products have the same viewing geometry, i.e.

372 they measure the whole troposphere. The ground-based products in Hefei are verified

373 to be robust in troposphere (section 3) and the HCHO product is dedicated to future

374 satellite validation (Vigouroux et al., 2018).

375 Second, while in most previous studies tropospheric NO_2 and total HCHO have

376 been chosen as the proxy (Martin et al., 2004; Duncan et al., 2010; Witte et al., 2011;

377 Jin and Holloway, 2015; Jin et al., 2017), we used the same tropospheric limits for all

378 gases to calculate tropospheric columns. The AVK's of the measurements show, that

379 all three gases are sensitive throughout the troposphere (compare figure S2).

380 Third, most previous studies used chemical transport model to estimate the

381 transition threshold (Martin et al., 2004a; Duncan et al., 2010; Witte et al., 2011; Jin

382 and Holloway, 2015; Schroeder et al., 2017; Jin et al., 2017). We used the observation

383 results plus an empirical iterative scheme to calculate the transition threshold (Su et

384 al., 2017). Schroeder et al. (2017) showed, that the transition threshold depends on the

385 particular conditions of the site under study and no global value can be obtained.

386 Since the measurement tools for O_3 and HCHO, the pollution characteristic and

387 the meteorological condition in this study were not the same as those of previous

388 studies, the transition thresholds estimated in either previous studies were not

389 straightly applied here (Martin et al., 2004a; Duncan et al., 2010; Witte et al., 2011;

390 Choi et al., 2012; Jin and Holloway, 2015; Mahajan et al., 2015; Schroeder et al.,

391 2017; Jin et al., 2017). In order to determine transition thresholds applicable in Hefei,

392 China, we iteratively altered the column $HCHO/NO_2$ ratio threshold and judged

393 whether the sensitivities of tropospheric O_3 to HCHO or NO_2 changed abruptly. For

394 example, in order to estimate the VOC-limited threshold, we first fitted tropospheric

395 O_3 to HCHO that lies within column $HCHO/NO_2$ ratios < 2 (an empirical start point)

396 to obtain the corresponding correlation/slope, and then we decreased the threshold by

397 0.1 (an empirical step size) and repeated the fit, i.e., only fitted the data pairs with

398 column $HCHO/NO_2$ ratios < 1.9. This has been done iteratively. Finally, we sorted

399 out the transition ratio which shows an abrupt change in correlation/slope, and

400 regarded this as the VOC-limited threshold. Similarly, the NO_x-limited threshold was

401 determined by iteratively increasing the column $HCHO/NO_2$ ratio threshold till the

402 sensitivity of tropospheric O_3 to NO_2 changed abruptly.

403   The transition threshold estimation using this scheme exploits the fact that O_3

404 production is more sensitive to VOCs if it is VOCs-limited and is more sensitive to

405 NO_x if it is NO_x limited, and it exists a transition point near the threshold (Martin et

406 al., 2004). Su et al. (2017) used this scheme to investigate the O_3-NOx-VOCs

407 sensitivities during the 2016 G20 conference in Hangzhou, China, and argued that this

408 diagnosis of PO_3 could reflect the overall O_3 production conditions.

409 5.3.2 PO_3 limitations in Hefei

410   The FTS retrievals within ± 1 h of OMI overpass time (13:30 local time (LT))

411 were used for investigation of PO_3 limitations. While the FTS instrument can measure

412 throughout the whole day, if not cloudy, OMI measures only during midday. For

413 Hefei, this coincidence criterion is a balance between the accuracy and the number of

414 data points. Through the above empirical iterative calculation, we observed a

415 VOC-limited regime with column $HCHO/NO_2$ ratios < 1.3, a NOx-limited regime

with column HCHO/NO_2 ratios > 2.8, and a mix VOC-NO_x-limited regime with column HCHO/NO_2 ratios between 1.3 and 2.8. Schroeder et. al. (2017) argued, the column measurements from space have to be used with care because of the high uncertainty and the inhomogeneity of the satellite measurements. This has been mitigated in this study by the following:

The FTIR measurements have a much smaller footprint than the satellite measurements. Also we concentrate on measurements recorded during midday, when the mixing layer has largely been dissolved.

The measurements are more sensitive to the lower parts of the troposphere, which can be inferred from the normalized AVK's. This reason is simply, that the AVK's show the sensitivity to the column, but the column per altitude decreases with altitude.

Figure 7 shows time series of column HCHO/NO_2 ratios which varied over a wide range from 1.0 to 9.0. The column HCHO/NO_2 ratios in summer are typically larger than those in winter, indicating that the PO_3 is mainly NO_x limited in summer and mainly VOC limited or mix VOC-NO_x limited in winter. Based on the calculated transition criteria, 106 days of observations that have coincident O_3, HCHO, and NO_2 counterparts in the reported period are classified, where 57 days (53.8%) are in MAM/JJA season and 49 days (46.2%) are in SON/DJF season. Table 4 listed the statistics for the 106 days of observations, which shows that NO_x limited, mix VOC-NO_x limited, and VOC limited PO_3 accounts for 60.3% (64 days), 28.3% (30 days), and 11.4% (12 days), respectively. The majority of NO_x limited (70.3%) PO_3 lies in MAM/JJA season, while the majorities of mix VOC-NO_x limited (70%) and VOC limited (75%) PO_3 lie in SON/DJF season. As a result, reductions in NO_x and VOC could be more effective to mitigate O_3 pollution in MAM/JJA and SON/DJF season, respectively. Furthermore, considering most of PO_3 are NO_x limited or mix VOC-NO_x limited, reductions in NO_x would reduce most O_3 pollution in eastern China.

6 Conclusion

We investigated the seasonal evolution and photochemical production regime of

445   tropospheric O_3 in eastern China from 2014 – 2017 by using tropospheric O_3, CO and

446   HCHO columns derived from Fourier transform infrared spectrometry (FTS),

447   tropospheric NO_2 column deduced from Ozone Monitoring Instrument (OMI), the

448   surface meteorological data, and a back trajectory cluster analysis technique. A

449   pronounced seasonal cycle for tropospheric O_3 is captured by the FTS, which roughly

450   increases over time at the first half year and reaches the maximum in June, and then it

451   decreases over time at the second half year. Tropospheric O_3 columns in June are, on

452   average, 0.50×10^{18} molecules*cm^{-2} (47.6%) higher than those in December which has

453   a mean value of 1.05×10^{18} molecules*cm^{-2}. A broad maximum within both spring and

454   summer (MAM/JJA) is observed and the day-to-day variations in MAM/JJA are

455   generally larger than those in autumn and winter (SON/DJF). This differs from

456   tropospheric O_3 measurements in Vigouroux et al. (2015). However, Vigouroux et al.

457   (2015) used measurements at relatively clean sites.

458   Back trajectories analysis showed that air pollution in Jiangsu and Anhui

459   Province in eastern China, Hebei and Shandong Province in northern China, Shaanxi,

460   Henan and Shanxi Province in northwest China, Hunan and Hubei Province in central

461   China dominate the contributions to the observed tropospheric O_3 levels. Compared

462   with SON/DJF season, the observed tropospheric O_3 levels in MAM/JJA are mainly

463   influenced by transport of air masses from densely populated and industrialized areas

464   while the broad and high O_3 level and variability in MAM/JJA is determined by the

465   photochemical O_3 production. The tropospheric column HCHO/NO_2 ratio is used as a

466   proxy to investigate the chemical sensitivity of O_3 production rate (PO$_3$). The results

467   show that the PO$_3$ is mainly nitrogen oxide (NO_x) limited in MAM/JJA, while it is

468   mainly VOC or mix VOC-NO_x limited in SON/DJF. Reductions in NO_x and VOC

469   could be more effective to mitigate O_3 pollution in MAM/JJA and SON/DJF season,

470   respectively. Considering most of PO$_3$ are NO_x limited or mix VOC-NO_x limited,

471   reductions in NO_x would reduce most O_3 pollution in eastern China.

472   **Acknowledgements**

473   This work is jointly supported by the National High Technology Research and

Development Program of China (No. 2016YFC0200800, No. 2017YFC0210002, No. 2016YFC0203302), the National Science Foundation of China (No. 41605018, No. 41405134, No.41775025, No. 41575021, No. 51778596, No. 91544212, No. 41722501, No. 51778596), Anhui Province Natural Science Foundation of China (No. 1608085MD79), Outstanding Youth Science Foundation (No. 41722501) and the German Federal Ministry of Education and Research (BMBF) (Grant No. 01LG1214A). The processing and post processing environment for SFIT4 are provided by National Center for Atmospheric Research (NCAR), Boulder, Colorado, USA. The NDACC networks are acknowledged for supplying the SFIT software and advice. The HCHO micro-windows were obtained at BIRA-IASB during the ESA PRODEX project TROVA (2016-2018) funded by the Belgian Science Policy Office. We thank University of Wollongong for their guidance with respect to instrument alignment and site operation. The LINEFIT code is provided by Frank Hase, Karlsruhe Institute of Technology (KIT), Institute for Meteorology and Climate Research (IMK-ASF), Germany. The authors acknowledge the NOAA Air Resources Laboratory (ARL) for making the HYSPLIT transport and dispersion model available on the Internet. The authors would also like to thank Dr. Jason R. Schroeder and three anonymous referees for useful comments that improved the quality of this paper.

References

Albrecht T., Notholt J., Wolke R., Solberg S., Dye C., Malberg H., Variations of CH_2O and C_2H_2 determined from ground based FTIR measurements and comparison with model results, Adv. Space Res., 29, p. 1713-1718, 2002.

Boersma, K. F., D. J. Jacob, M. Trainic, Y. Rudich, I. DeSmedt, R. Dirksen, and H. J. Eskes (2009), Validation of urban NO_2 concentrations and their diurnal and seasonal variations observed from the SCIAMACHY and OMI sensors using in situ surface measurements in Israeli cities, Atmos. Chem. Phys., 9(12), 3867–3879, doi:10.5194/acp-9-3867-2009.

Choi, Y., H. Kim, D. Tong, and P. Lee (2012), Summertime weekly cycles of observed and modeled NOx and O_3 concentrations as a function of satellite-derived ozone

production sensitivity and land use types over the continental United States, Atmos. Chem. Phys., 12(14), 6291–6307, doi:10.5194/acp-12-6291-2012.

Coates J., Mar K. A., Ojha N., Butler T. M.. The influence of temperature on ozone production under varying NOx conditions - a modelling study. Atmospheric Chemistry and Physics. 2016,16(18):11601-15.

Duncan, B.N., et al., 2010. Application of OMI observations to a space-based indicator of NO_x and VOC controls on surface ozone formation. Atmos. Environ. 44, 2213-2223.

Draxler, R. R., Stunder, B., Rolph, G., and Taylor, A.: HYSPLIT_4 User's Guide, via NOAA ARL website. NOAA Air Resources Laboratory, Silver Spring, MD, December 1997, revised January 2009, http://www.arl.noaa.gov/documents/ reports/hysplit_user_guide.pdf (last access: 19 May 2017), 2009.

Edwards, P. M., Young, C. J., Aikin, K., & Degouw, J. A. (2013). Ozone photochemistry in an oil and natural gas extraction region during winter: simulations of a snow-free season in the uintah basin, utah. Atmospheric Chemistry & Physics, 13(17), 8955-8971.

Franco B., Hendrick F., Van Roozendael M., Muller J. F., Stavrakou T., Marais E. A., Retrievals of formaldehyde from ground-based FTIR and MAX-DOAS observations at the Jungfraujoch station and comparisons with GEOS-Chem and IMAGES model simulations. Atmospheric Measurement Techniques. 2015, 8(4):1733-56.

Gardiner, T., Forbes, A., de Mazière, M., Vigouroux, C., Mahieu, E., Demoulin, P., Velazco, V., Notholt, J., Blumenstock, T., Hase, F., Kramer, I., Sussmann, R., Stremme,W., Mellqvist, J., Strandberg, A., Ellingsen, K., and Gauss, M.: Trend analysis of greenhouse gases over Europe measured by a network of ground-based remote FTIR instruments, Atmos. Chem. Phys., 8, 6719–6727, doi:10.5194/ acp-8-6719-2008, 2008.

Hase, F.: Improved instrumental line shape monitoring for the ground-based, high-resolution FTIR spectrometers of the Network for the Detection of Atmospheric Composition Change, Atmos. Meas. Tech., 5, 603–610,

533   doi:10.5194/amt-5-603-2012,2012.

534 Jin, X., and T. Holloway (2015), Spatial and temporal variability of ozone sensitivity

535   over China observed from the Ozone Monitoring Instrument, J. Geophys. Res.

536   Atmos., 120, 7229–7246, doi:10.1002/2015JD023250.

537 Jin X. M., Fiore A.M., Murray L.T., Valin L.C., Lamsal L.N., Duncan B. Evaluating a

538   Space-Based Indicator of Surface Ozone-NOx-VOC Sensitivity Over Midlatitude

539   Source Regions and Application to Decadal Trends. J Geophys Res-Atmos.

540   2017,122(19):10231-53.

541 Jones N.B., Riedel K., Allan W., Wood S., Palmer P.I., Chance K., et al. Long-term

542   tropospheric formaldehyde concentrations deduced from ground-based fourier

543   transform solar infrared measurements. Atmos Chem Phys. 2009,9(18):7131-42.

544 Kleinman, L., Daum, P., Lee, Y.-N., Nunnermacker, L., Springston, S., Weinstein-

545   Lloyd, J., Rudolph, J., 2005. A comparative study of ozone production in five

546   U.S. metropolitan areas. Journal of Geophysical Research 110, D02301.

547   doi:10.1029/2004JD005096.

548 Kalnay E., Kanamitsu M., Kistler R., et al. (1996) The NCEP/NCAR 40-year

549   reanalysis project. Bulletin of the American Meteorological Society, 77, 437-472.

550 Lei W., Zavala M., de Foy B., Volkamer R., Molina L. T.. Characterizing ozone

551   production and response under different meteorological conditions in Mexico City.

552   Atmospheric Chemistry and Physics. 2008, 8(24):7571-81.

553 Martin, R., Fiore, A., Van Donkelaar, A., 2004a. Space-based diagnosis of surface

554   ozone sensitivity to anthropogenic emissions. Geophysical Research Letters 31,

555   L06120. doi:10.1029/2004GL019416.

556 Martin, R., Parrish, D., Ryerson, T., Nicks, D., Chance, K., Kurosu, T., Jacob, D.,

557   Sturges, E., Fried, A., Wert, B., 2004b. Evaluation of GOME satellite

558   measurements of tropospheric NO_2 and HCHO using regional data from aircraft

559   campaigns in the southeastern United States. Journal of Geophysical Research

560   109, D24307. doi:10.1029/2004JD004869.

561 Millet, D. B., D. J. Jacob, K. F. Boersma, T.-M. Fu, T. P. Kurosu, K. Chance, C. L.

562   Heald, and A. Guenther (2008), Spatial distribution of isoprene emissions from

North America derived from formaldehyde column measurements by the OMI satellite sensor, J. Geophys. Res., 113, D02307, doi:10.1029/2007JD008950.

Mahajan, A. S., I. De Smedt, M. S. Biswas, S. Ghude, S. Fadnavis, C. Roy, and M. van Roozendael (2015), Inter-annual variations in satellite observations of nitrogen dioxide and formaldehyde over India, Atmos. Environ., 116, 194–201, doi:10.1016/j.atmosenv.2015.06.004.

Oltmans S. J., Lefohn A. S., Harris J. M., et al. Long-term changes in tropospheric ozone. Atmospheric Environment, 2006, 40(17):3156-3173.

Rothman, L. S., Gordon, I. E., Barbe, A., Benner, D. C., Bernath, P. F., Birk, M., Boudon, V., Brown, L. R., Campargue, A., Champion, J.-P., Chance, K., Coudert, L. H., Danaj, V., Devi, V. M., Fally, S., Flaud, J.-M., Gamache, R. R., Goldmanm, A., Jacquemart, D., Kleiner, I., Lacome, N., Lafferty, W. J., Mandin, J.-Y., Massie, S. T., Mikhailenko, S. N., Miller, C. E., Moazzen-Ahmadi, N., Naumenko, O. V., Nikitin, A. V., Orphal, J., Perevalov, V. I., Perrin, A., Predoi-Cross, A., Rinsland, C. P., Rotger, M., Šime. cková, M., Smith, M. A. H., Sung, K., Tashkun, S. A., Tennyson, J., Toth, R. A., Vandaele, A. C., and Vander Auwera, J.: The Hitran 2008 molecular spectroscopic database, J. Quant. Spectrosc. Ra., 110, 533–572, 2009.

Rubin, J. I., Kean, A. J., Harley, R. A., Millet, D. B., and Goldstein, A. H.: Temperature dependence of volatile organic compound evaporative emissions from motor vehicles, J. Geophys. Res.-Atmos., 111, d03305, doi:10.1029/2005JD006458, 2006.

Schroeder, J. R., Crawford, J. H., Fried, A., Walega, J., Weinheimer, A., & Wisthaler, A., et al. (2017). New insights into the column CH_2O/NO_2 ratio as an indicator of near‐surface ozone sensitivity. Journal of Geophysical Research Atmospheres, 122(16).

Sillman, S., 1995a. The use of NOy, H_2O_2, and HNO_3 as indicators for ozone-NO_x hydrocarbon sensitivity in urban locations. J. Geophys. Res. 100, 14175-14188.

Sillman, S. and Samson, P. J.: Impact of temperature on oxidant photochemistry in urban, polluted rural and remote environments, J. Geophys. Res.-Atmos., 100,

593   11497–11508, 1995b.

594 Stunder, B.: An assessment of the Quality of Forecast Trajectories, J. Appl. Meteorol.,

595   35, 1319–1331, 1996.

596 Streets, D. G., et al. (2013), Emissions estimation from satellite retrievals: A review of

597   current capability, Atmos. Environ., 77, 1011–1042,   doi:10.1016/j.atmosenv.

598   2013.05.051.

599 Su W. J., Liu C., Hu Q.H., Fan G.Q., Xie Z.Q., Huang X., Characterization of ozone in

600   the lower troposphere during the 2016 G20 conference in Hangzhou. Sci Rep-Uk.

601   2017,7.

602 Tang, G., Wang, Y., Li, X., Ji, D., & Gao, X. (2011). Spatial-temporal variations of

603   surface ozone and ozone control strategy for northern china. Atmospheric

604   Chemistry & Physics, 11(9), 26057-26109.

605 Tonnesen, G. S., and R. L. Dennis (2000), Analysis of radical propagation efficiency

606   to assess ozone sensitivity to hydrocarbons and NO_2. Long-lived species as

607   indicators of ozone concentration sensitivity, J. Geophys. Res., 105(D7),

608   9227–9241, doi:10.1029/1999JD900372.

609 Tian Y., Sun Y.W., Liu C., Wang W., Shan C. G., Xu X.W., Hu Q.H., Characterisation

610   of methane variability and trends from near-infrared solar spectra over Hefei,

611   China, Atmospheric Environment, Volume 173, 2018,   Pages   198-209,   ISSN

612   1352-2310, https://doi.org/10.1016/j.atmosenv.2017.11.001.

613 Vigouroux, C., Blumenstock, T., Coffey, M., Errera, Q., Garc á, O., Jones, N. B.,

614   Hannigan, J. W., Hase, F., Liley, B., Mahieu, E., Mellqvist, J., Notholt, J., Palm,

615   M., Persson, G., Schneider, M., Servais, C., Smale, D., Th ölix, L., and De Mazi ère,

616   M.: Trends of ozone total columns and vertical distribution from FTIR

617   observations at eight NDACC stations around the globe, Atmos. Chem. Phys., 15,

618   2915-2933, doi:10.5194/acp-15-2915-2015, 2015.

619 Vigouroux C., Hendrick F, Stavrakou T, et al. Ground-based FTIR and MAX-DOAS

620   observations of formaldehyde at R éunion Island and comparisons with satellite

621   and model data[J]. Atmospheric Chemistry & Physics, 2009, 9(4):9523-9544.

622 Vigouroux, C., Bauer Aquino, C. A., Bauwens, M., Becker, C.,Blumenstock, T., De

Mazière, M., Garciá, O., Grutter, M., Guarin, C.,Hannigan, J., Hase, F., Jones, N., Kivi, R., Koshelev, D., Langerock,B., Lutsch, E., Makarova, M., Metzger, J.-M., Muller, J.-F., Notholt,J., Ortega, I., Palm, M., Paton-Walsh, C., Poberovskii, A., Rettinger, M., Robinson, J., Smale, D., Stavrakou, T., Stremme, W., Strong, K., Sussmann, R., Té, Y., and Toon, G.: NDACC harmonized formaldehyde time-series from 21 FTIR stations covering a wide range of column abundances, Atmospheric Measurement Techniques Discussions, 2018, 1-30, https://www.atmos-meas-tech-discuss.net/amt-2018-22/,DOI=10.5194/amt-2018-22, 2018.

Witte, J.C., Duncan, B.N, Douglass, A.R, Kurosu, T.P, Chance, K et al. "The unique OMI HCHO/NO_2 feature during the 2008 Beijing Olympics: Implications for ozone production sensitivity". Atmospheric Environment. 45.18 2011-06-01. 3103(9).

Viatte C., Strong K., Walker K.A., Drummond J.R. Five years of CO, HCN, C_2H_6, C_2H_2, CH_3OH, HCOOH and H_2CO total columns measured in the Canadian high Arctic. Atmospheric Measurement Techniques. 2014;7(6):1547-70.

Wennberg, P. O., and Dabdub D. Atmospheric chemistry. Rethinking ozone production. Science 319.5870(2008):1624.

Wang T., Xue L. K., Brimblecombe P., Lam Y. F., Li. L., Zhang L. Ozone pollution in China: A review of concentrations, meteorological influences, chemical precursors, and effects. Sci Total Environ. 2017, 575:1582-96.

Wang W., Tian Y., Liu C., Sun Y., Liu W., Xie P., et al. Investigating the performance of a greenhouse gas observatory in Hefei, China. Atmos Meas Tech. 2017,10(7):2627-43.

Xing, C., Liu, C., Wang, S., Chan, K. L., Gao, Y., & Huang, X., et al. (2017). Observations of the vertical distributions of summertime atmospheric pollutants and the corresponding ozone production in shanghai, china. Atmospheric Chemistry & Physics, 17(23), 1-31.

651 **Figs**

652

653 (a)

654

655 (b)
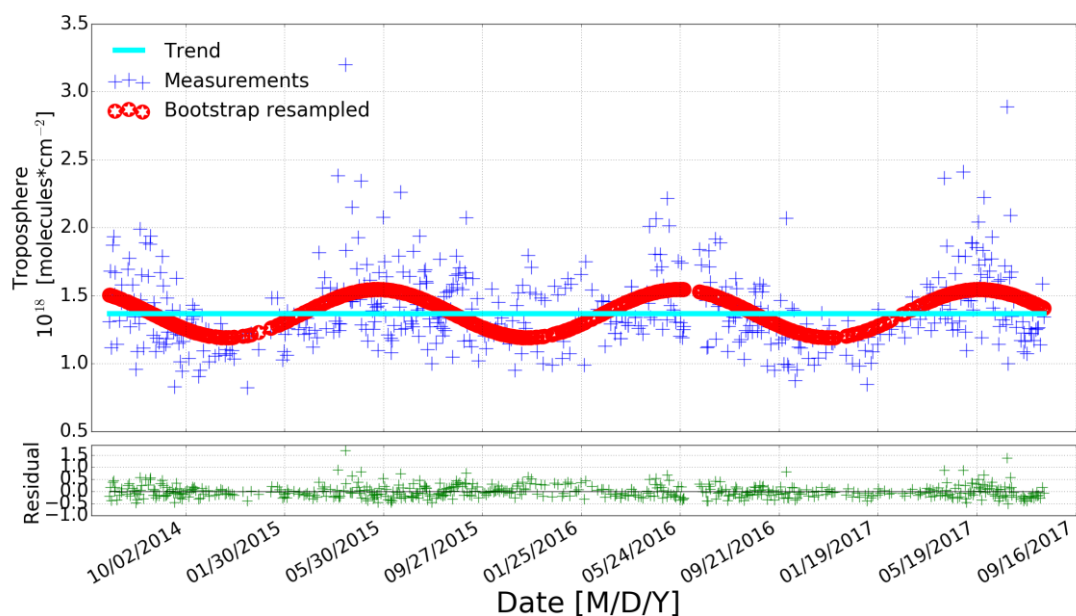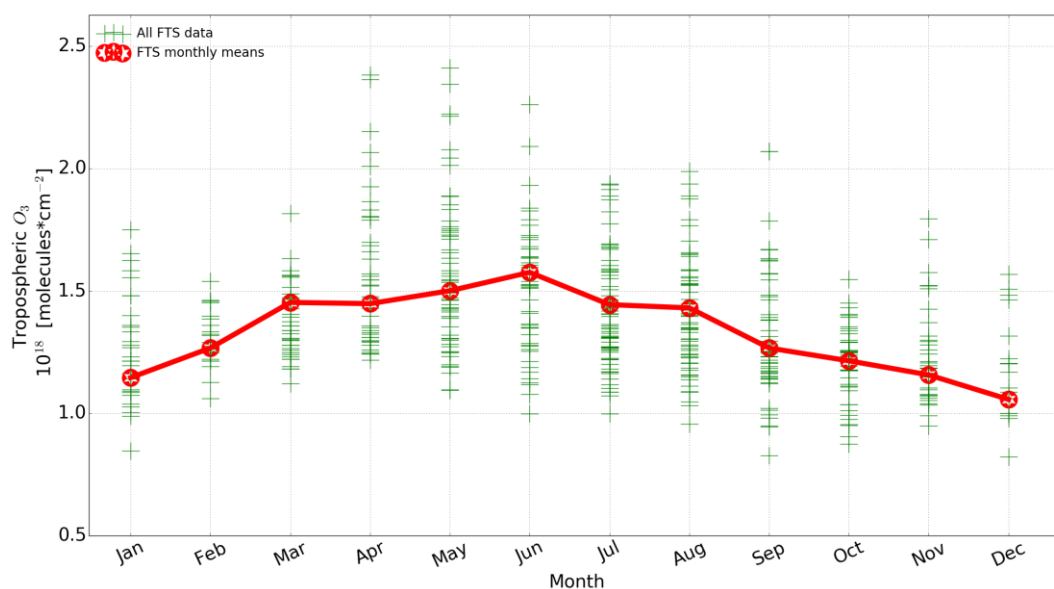
656 Figure 1. (a): FTS measured and bootstrap resampled tropospheric O_3 columns at Hefei site. The
657 linear trend and the residual are also shown. (b): Tropospheric O_3 column monthly means derived
658 from (a).

659

660   (a)

661

662   (b)
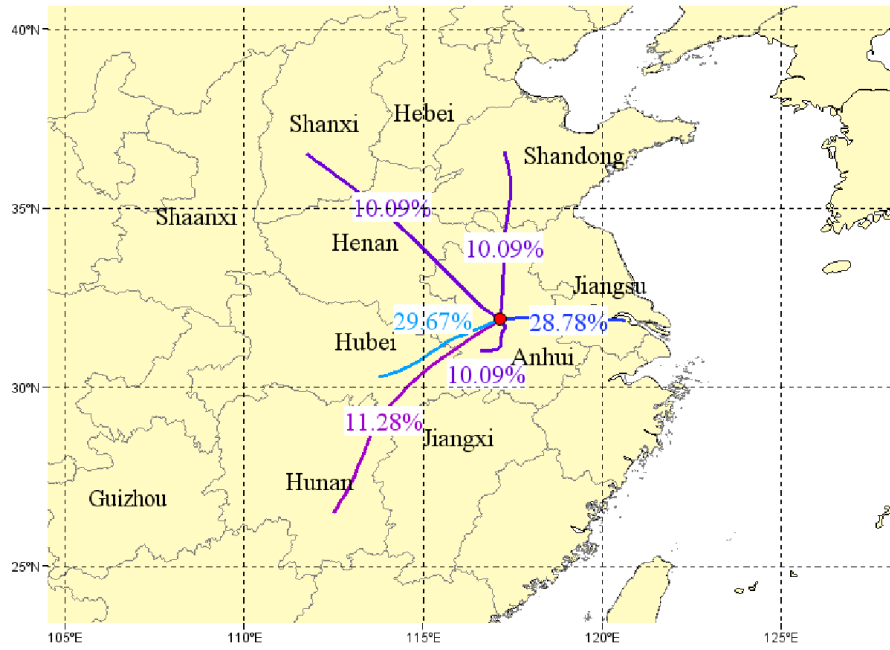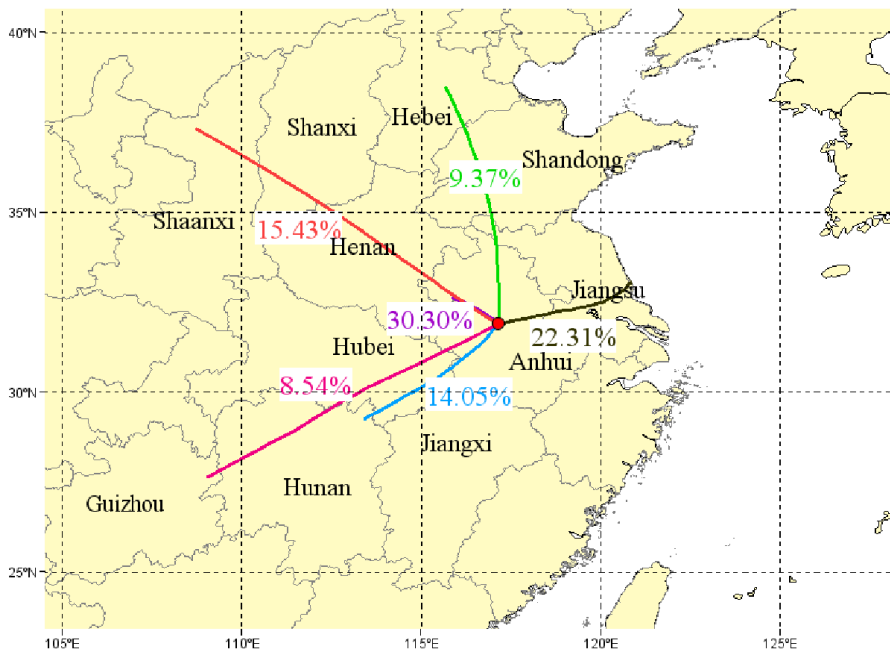
663   Figure 2. One-day HYSPLIT back trajectory clusters arriving at Hefei at 1500 m a.s.l that are

664   coincident with the FTS measurements from 2014 - 2017. (a) Spring and summer (MAM/JJA),

665   and (b) Autumn and winter (SON/DJF) season. The base map was generated using the TrajStat

666   1.2.2 software (http://www.meteothinker. com).

667
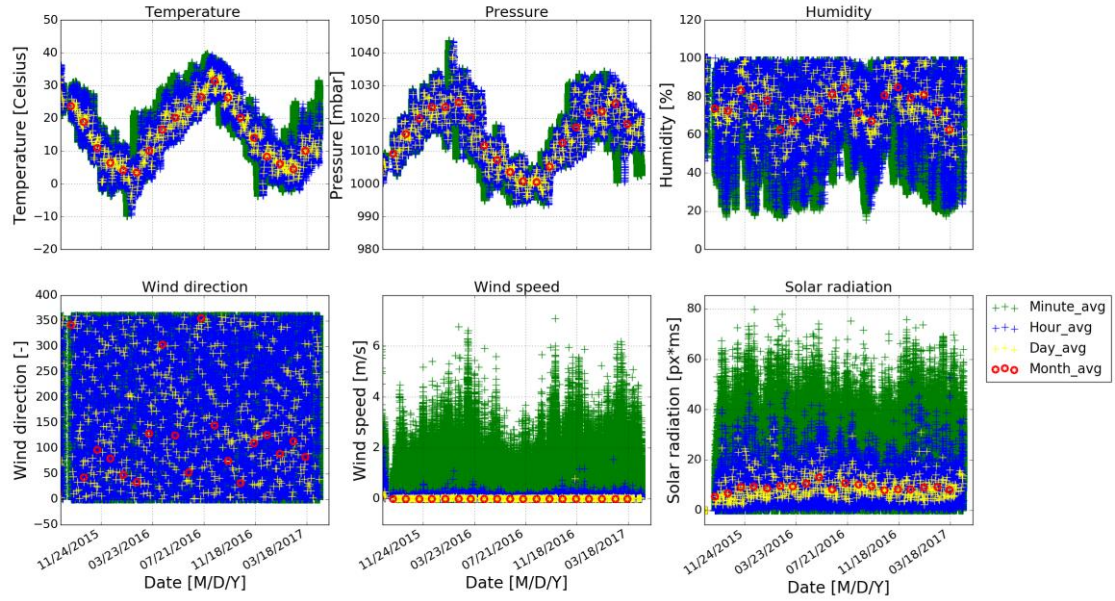
668 Figure 3. Minutely, hourly, daily, and monthly averaged time series of temperature, pressure,

669 humidity, wind direction, wind speed, and solar radiation recorded by the surface weather station.

670
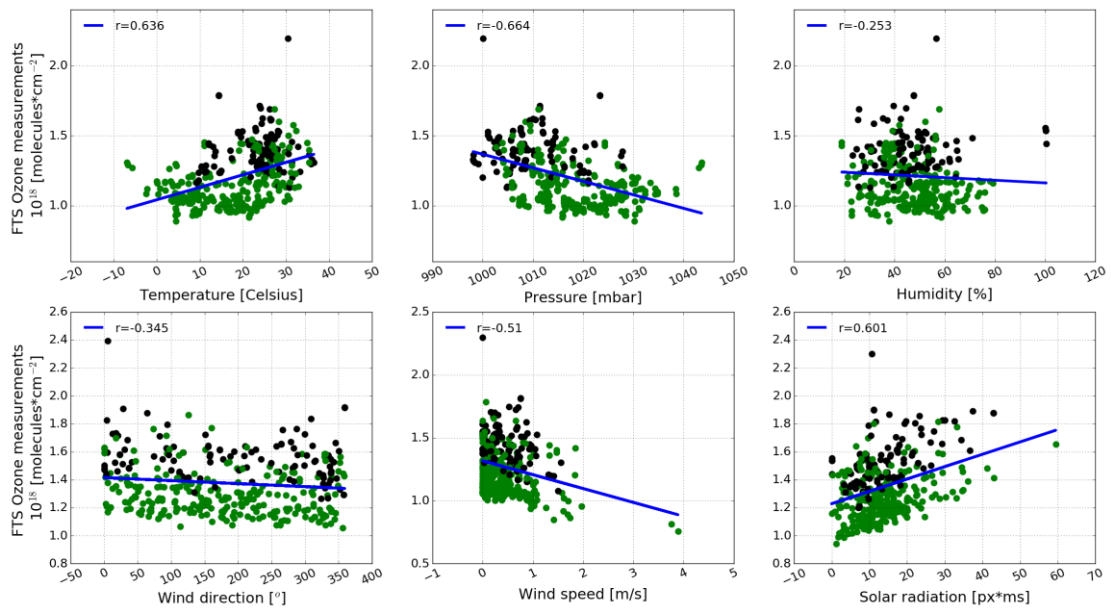
671 Figure 4. Correlation plot between the FTS tropospheric O_3 column and the coincident

672 minutely-averaged surface meteorological data. Black dots are data pairs within MAM/JJA season

673 and green dots are data pairs within SON/DJF season.

674
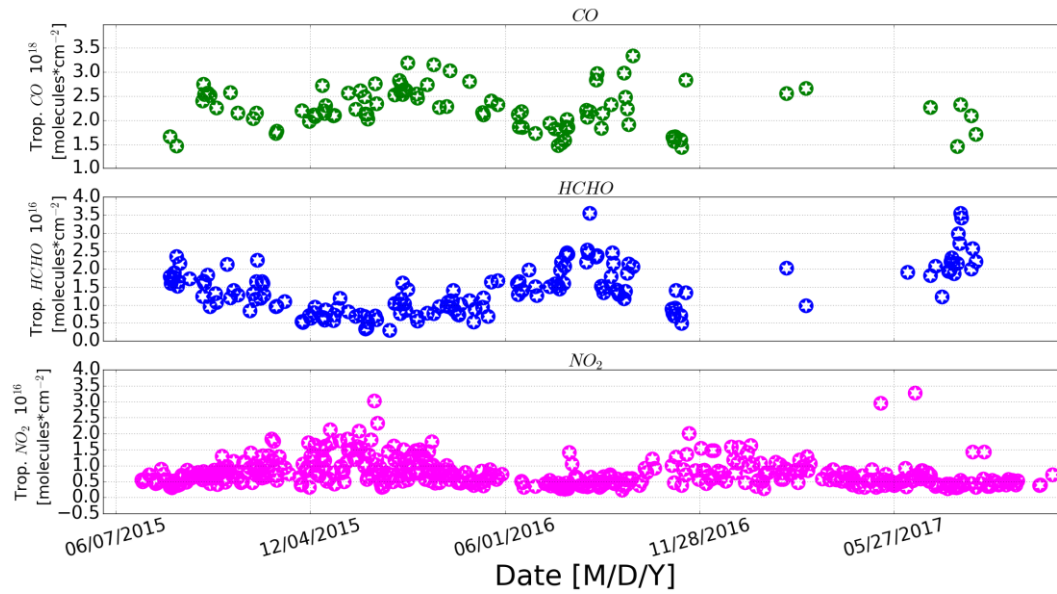
675 Figure 5. Time series of tropospheric CO, HCHO, and NO_2. Tropospheric CO and HCHO were

676 derived from FTS observations which is the same as tropospheric O_3 and tropospheric NO_2 is

677 derived from OMI data.

678

679

680

681

682
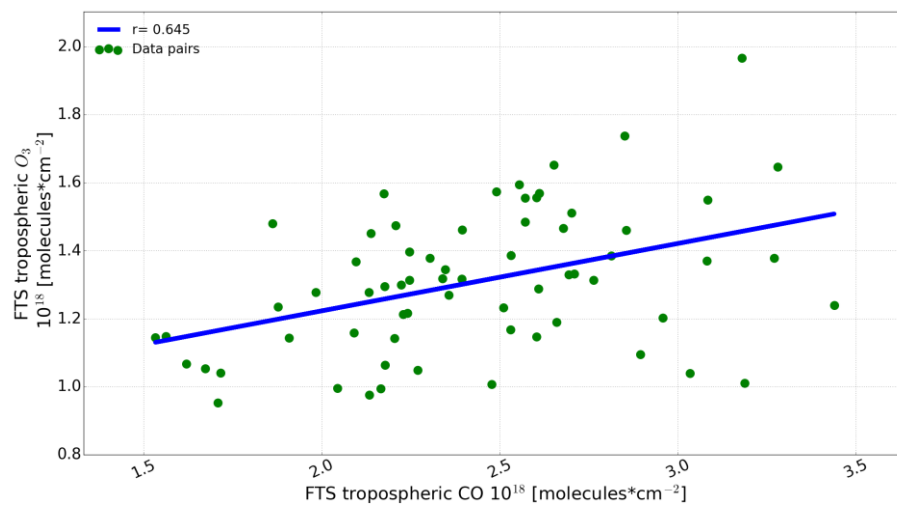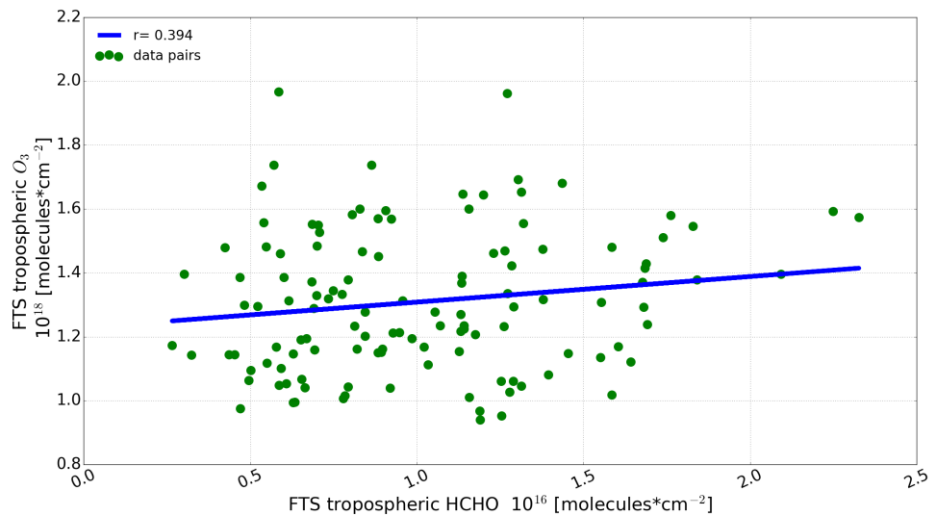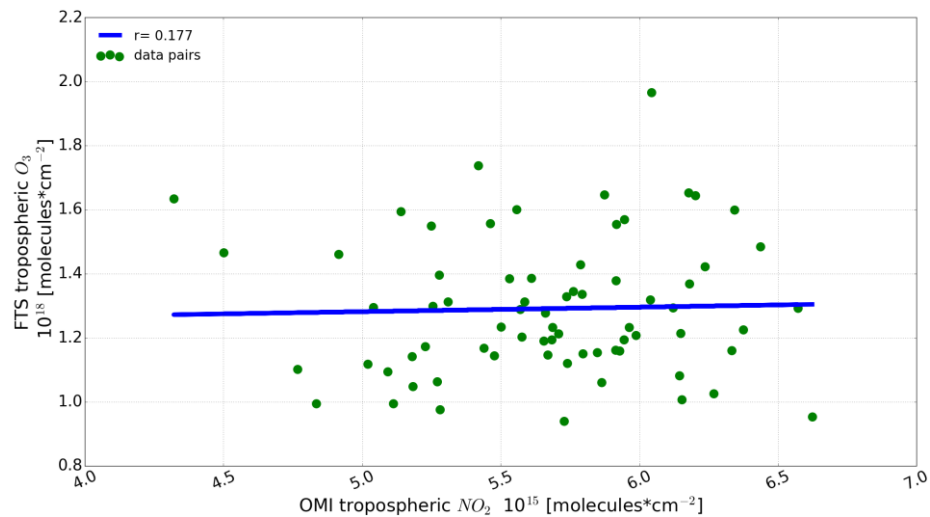
Figure 6. Correlation plot between the FTS tropospheric O_3 column and coincident tropospheric

CO (upper), HCHO (middle), and NO_2 (bottom) columns. The CO and HCHO data are retrieved

from FTS observations and the NO_2 data were deduced from OMI product.
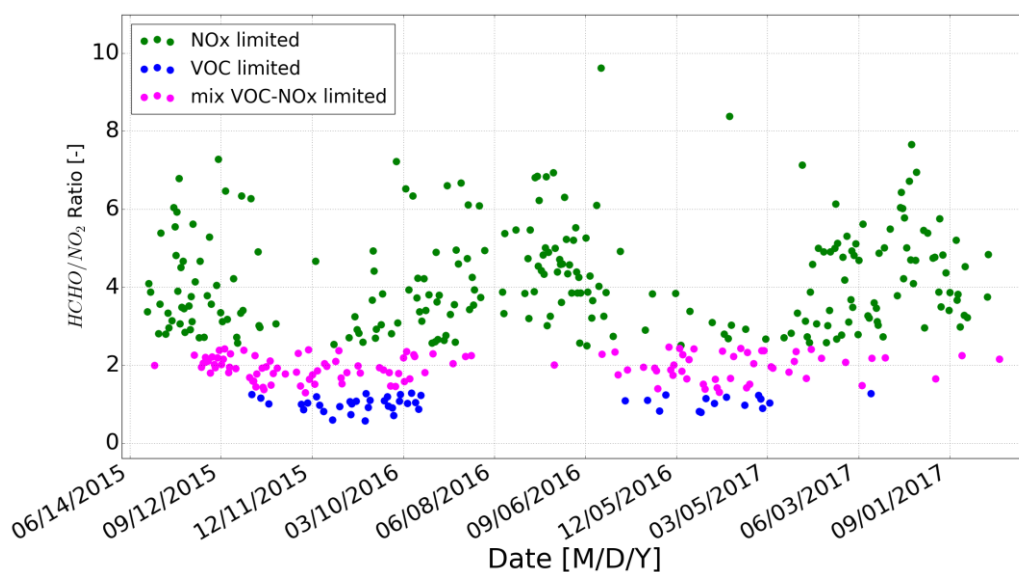
Figure 7. Time series of column HCHO/NO₂ ratios.

Tables

Table 1. Summary of the retrieval parameters used for O₃, CO, and HCHO. All micro windows (MW) are given in cm⁻¹.

Gases		O₃	CO	HCHO
Retrieval code		SFIT4 v 0.9.4.4	SFIT4 v 0.9.4.4	SFIT4 v 0.9.4.4
Spectroscopy		HITRAN2008	HITRAN2008	HITRAN2008
P, T, H₂O profiles		NCEP	NCEP	NCEP
A priori profiles for target/interfering gases except H₂O		WACCM	WACCM	WACCM
MW for profile retrievals		1000-1004.5	2057.7-2058 2069.56-2069.76 2157.5-2159.15	2763.42-2764.17 2765.65-2766.01 2778.15-2779.1 2780.65-2782.0
Retrieved interfering gases		H₂O, CO₂, C₂H₄, ⁶⁶⁸O₃, ⁶⁸⁶O₃	O₃, N₂O, CO₂, OCS, H₂O	CH₄, O₃, N₂O, HDO
SNR for de-weighting		None	500	600
Regularization	**S**ₐ	Diagonal: 20% No correlation	Diagonal: 11% ~ 27% No correlation	Diagonal: 10% No correlation
	Sε	Real SNR	Real SNR	Real SNR
ILS		LINEFIT145	LINEFIT145	LINEFIT145
Error analysis		Systematic error: -Smoothing error (smoothing) -Errors from other parameters: Background curvature (curvature), Optical path difference (max_opd), Field of view (omega), Solar line strength (solstrnth), Background slope (slope), Solar line shift (solshft), Phase (phase), Solar zenith angle(sza), Line temperature broadening (linetair_gas), Line pressure broadening (linepair_gas), Line intensity(lineint_gas)		
		Random error: -Interference errors: retrieval parameters (retrieval_parameters), interfering species (interfering_species) -Measurement error (measurement) - Errors from other parameters: Temperature (temperature), Zero level (zshift)		

697
698 Table 2. Typical degrees of freedom for signal (DOFs) and sensitive range of the retrieved O$_3$, CO, and HCHO profiles at Hefei site.

Gas	Total column DOFs	Sensitive range (km)	Tropospheric partial column (km)	Tropospheric DOFs
O$_3$	4.8	Ground - 44	Ground - 12	1.5
CO	3.5	Ground - 27	Ground - 12	2.7
HCHO	1.2	Ground - 18	Ground - 12	1.1

699

700 Table 3. Errors in % of the column amount of O$_3$, CO, and HCHO for 0 − 12 km tropospheric partial column and
701 for the total column.

Gas	O$_3$		CO		HCHO	
Altitude (km)	0 − 12	Total column	0 − 12	Total column	0 − 12	Total column
Total random	3.2	0.59	3.8	0.66	3.3	0.97
Total systematic	8.1	4.86	5.7	3.9	9.6	5.7
Total errors	8.7	5.0	6.8	3.95	10.2	5.8

702

703

704 Table 4. Chemical sensitivities of PO$_3$ for the selected 106 days of observations that have coincident O$_3$, HCHO,
705 and NO$_2$ counterparts

Items	Proportion		Autumn and winter		Spring and summer	
	days	percentage	days	percentage	days	percentage
NOx limited	64	60.3%	19	29.7%	45	70.3%
Mix VOC-NOx limited	30	28.3%	21	70%	9	30%
VOC limited	12	11.4%	9	75%	3	25%
Sum	106	100%	49	46.2%	57	53.8%

706
707